Joule

CellPress

Article

Designing interphases for highly reversible aqueous zinc batteries

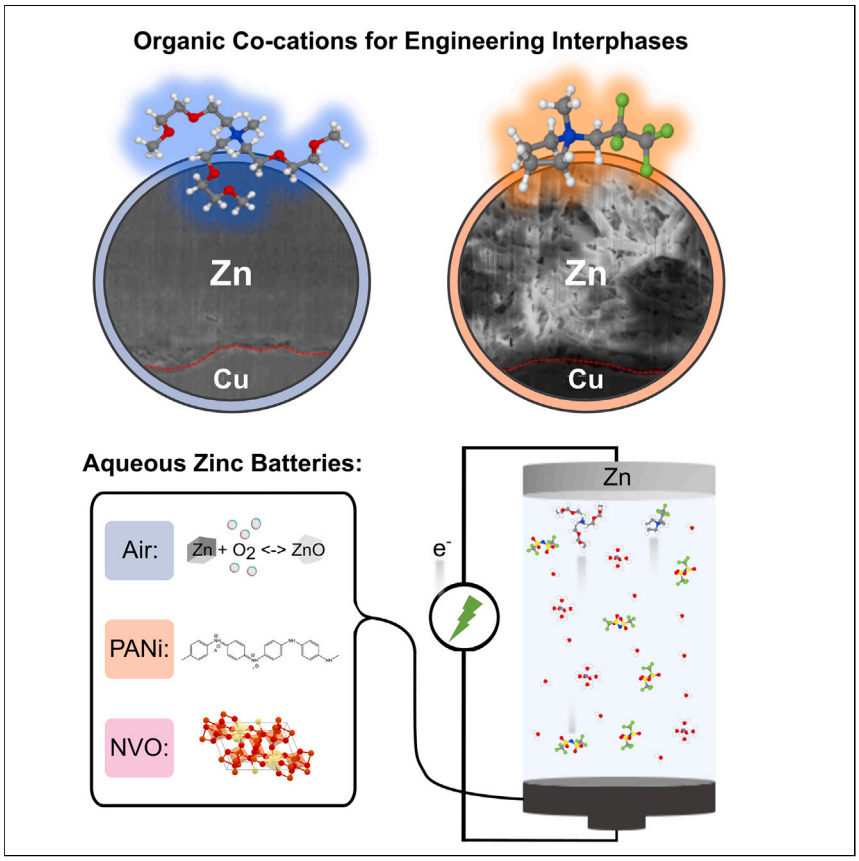

Two functionalized cations improve zinc metal anode reversibility in aqueous electrolyte by distinct mechanisms: a partially fluorinated pyrrolidinium cation strongly suppresses parasitic reactions such as hydrogen evolution, and an ether-functionalized ammonium cation supports more uniform zinc stripping and plating, thereby limiting dendrite formation. The co-cations also improve performance in zinc metal batteries featuring three types of cathodes (air, organic, and inorganic), indicating that this is a promising approach to address metal anode reversibility in next-generation batteries.

Glenn R. Pastel, Travis P. Pollard, Qian Liu, ..., Marshall A. Schroeder, Zhengcheng Zhang, Kang Xu

glenn.r.pastel.civ@army.mil

Highlights

We designed organic co-cations to improve Zn metal anode interphases

A partially fluorinated pyrrolidinium cation strongly suppresses parasitic reactions

An ether-functionalized ammonium cation supports dendrite suppression

The co-cations improve Zn metal batteries with three types of cathodes

Pastel et al., Joule 8, 1–13
April 17, 2024 Published by Elsevier Inc.
https://doi.org/10.1016/j.joule.2024.02.002

Please cite this article in press as: Pastel et al., Designing interphases for highly reversible aqueous zinc batteries, Joule (2024), https://doi.org/10.1016/j.joule.2024.02.002

Joule

CellPress

Article

Designing interphases for highly reversible aqueous zinc batteries

Glenn R. Pastel,[1,6,*] Travis P. Pollard,[1] Qian Liu,[2] Sydney Lavan,[2] Qijia Zhu,[2] Rongzhong Jiang,[1] Lin Ma,[3,4] Justin Connell,[2] Oleg Borodin,[1] Marshall A. Schroeder,[1] Zhengcheng Zhang,[2] and Kang Xu[5]

SUMMARY

Recent efforts to improve zinc metal anode reversibility in aqueous electrolytes have primarily focused on tailoring Zn^{2+} solvation. We propose a complementary approach to directly engineer the anode interphase with the help of two co-cations. The designed organic co-cations offer distinct improvements: a partially fluorinated pyrrolidinium cation effectively suppresses parasitic reactions such as hydrogen evolution (<6 μA cm^{-2}), while an ether-functionalized ammonium cation inhibits dendrite formation (almost 10 Ah cm^{-2} cumulative capacity, >1 year, Zn||Zn). Only 3 wt % of the co-cation combination enables full utilization of a 5-mAh cm^{-2} reservoir with over 99% Coulombic efficiency and 1,000 cycles with 20% reservoir utilization. We further validate this concept in Zn metal batteries with various cathode chemistries (O_2, polyaniline, and $HNaV_6O_{16}$), and we have achieved significant enhancements in performance. This suggests co-cations are a promising and universal approach to improve metal anode reversibility across emerging battery chemistries.

CONTEXT & SCALE

Lithium-ion battery supply chain and sustainability concerns are driving interest in alternative battery chemistries based on zinc (Zn) metal anodes; however, challenges related to parasitic side reactions and reversibility persist. In this work, we designed two functionalized co-cations that offer distinct and complementary benefits in aqueous Zn electrolyte: a partially fluorinated pyrrolidinium cation strongly suppresses parasitic reactions such as hydrogen evolution and forms tortuous deposits, while an ether-functionalized ammonium cation supports more uniform stripping and plating, thereby limiting dendrite formation. At additive levels, these heteroatomic cations can address several concerns related to metal anode reversibility, as evidenced from compelling full-cell performance with three promising cathode materials. This work demonstrates that organic cations can become a keystone of future high-performance electrolytes.

INTRODUCTION

Aqueous zinc batteries have the potential to ease supply chain and geopolitical concerns often associated with lithium-ion battery materials, but Zn anode utilization, reversibility, and cathode performance issues must first be resolved.[1–3] Numerous recent efforts focus on engineering the active cation solvation environment in the hope that an anion or co-solvent in the solvation sheath can introduce new interfacial and interphasial properties.[4,5] However, the Zn^{2+} solvation sheath in aqueous electrolytes has proven to be stubbornly populated with water molecules, despite leveraging high salt concentrations.[6] Other modifications in electrolyte composition tend to incur additional issues associated with manufacturing, environmental-friendliness, and cost (Table S1; Figure S1).[7–15]

In this work, we show that the electrochemical performance of Zn aqueous electrolytes can be directly and efficiently controlled via interphase engineering with additive-level co-cations, instead of altering the Zn^{2+} solvation sheath. Two such co-cations were synthesized based on our current understanding of interfacial and interphase design. The first, 1-methyl-1-(2,2,3,3,3-pentafluoropropyl)pyrrolidinium bis(trifluoromethylsulfonyl)imide (PfPyr), consists of a pyrrolidinium cation carrying a fluorinated alkyl coupled with an imide anion; the second, tris(3,6-dioxaheptanyl)(methyl)ammonium bis(trifluoromethylsulfonyl)imide (TDMA), consists of an ammonium cation with three ether linkages coupled with the same imide anion. While fluorinated anions and solvent molecules have been extensively investigated and

Please cite this article in press as: Pastel et al., Designing interphases for highly reversible aqueous zinc batteries, Joule (2024), https://doi.org/10.1016/j.joule.2024.02.002

applied in commercial electrolytes due to the apparent benefits of fluorinated species on electrochemical performance,[16,17] fluorinated cations are seldom reported because they are rare and difficult to synthesize.[18,19] However, from the perspective of interphase design, a fluorinated cation is better suited to contribute fluorine to the anode interphase than a fluorinated anion or solvent molecule.[20] Ether linkages contribute to relatively high reductive stability and low chemical reactivity in solvents, but as functional groups on a cation, their impact on anode interfacial behavior is unknown.[21] By comparing these co-cations in isolation and in combination, we identified their respective interfacial effects: the fluorinated pyrrolidinium cation effectively suppresses parasitic reactions including hydrogen evolution (HER) and simultaneously produces a highly porous morphology, while the ammonium cation with ether linkages effectively prevents dendrite formation, resulting in a dense, non-porous Zn^0 morphology. Using them together, we observe a blend of properties, which enable unprecedented battery performance including full utilization of a 5 mAh cm^{-2} Zn^0 reservoir, high Coulombic efficiencies, and excellent reversibility in aqueous electrolytes across various Zn cathode chemistries. With this small change in electrolyte composition ($\leq$3 wt %), we show significant improvements in performance. This demonstrates a promising strategy to engineer a new class of co-cation electrolyte species tailored for the metal anode in next-generation batteries.

RESULTS

Dendrite suppression

Using Zn||Zn symmetric cells cycled at 1 mA cm^{-2} and 1 mAh cm^{-2} (Figure 1A) and compared with a baseline electrolyte consisting of 3.8 molal (m) of zinc bis(trifluoromethane) sulfonyl imide ($Zn(TFSI)_2$) dissolved in water, we first evaluate the effectiveness of these co-cations separately. Relative to the state-of-the-art alkaline electrolytes, the baseline composition serves as a more stringent reference because it provides substantial improvements in reversibility, although dendrite growth still leads to cell failure after 70 h with 36 mV average stripping and plating overpotential. With the addition of 1 wt % of PfPyr, the lifetime of symmetric cells doubles under the same conditions with a slightly lower average overpotential of 27 mV (Figures 1B and S2). However, the deposition morphology remains poor as validated during post-mortem characterization in subsequent sections. In comparison, 2 wt % of TDMA drastically improves the cycle lifetime to well over 1 year, reaching almost 5,000 cycles or 10 Ah cm^{-2} cumulative capacity, while increasing the average overpotential to around 83 mV. This improvement hints at a change in deposition and stripping morphology at a commercially relevant rate. Combining these two co-cations under the same conditions leads to favorable performance with long lifetimes but higher stripping overpotentials (~3,500 h and 90 mV, respectively). Electrochemical impedance spectroscopy (EIS) and voltage profile analysis preclude the existence of soft shorts in the longest lasting cells with TDMA (Figures S3–S5). This initial test identifies a substantial reduction in dendrite susceptibility of Zn^0 with TDMA and overpotential improvements with PfPyr.

Parasitic current

Slow linear sweep voltammetry (LSV) scans on a stainless-steel working electrode and Tafel measurements on a zinc electrode indicate reduced parasitic current in the presence of 1 wt % PfPyr (Figures 1E and S6–S9; Table S2). More specifically, PfPyr suppresses HER and other reductive reactions to <10 μA cm^{-2} before the Zn plating potential, which is an unprecedented improvement over the baseline by more than an order in magnitude (Figure 1F). Additionally, the redox potential and stability window of the PfPyr electrolyte is shifted to more negative values,

[1]Battery Sciences Branch, DEVCOM Army Research Laboratory, Adelphi, MD 20783, USA

[2]Chemical Sciences and Engineering Division, Argonne National Laboratory, Lemont, IL 60439, USA

[3]Department of Mechanical Engineering and Engineering Science, University of North Carolina at Charlotte, Charlotte, NC 28223, USA

[4]Battery Complexity, Autonomous Vehicle and Electrification (BATT CAVE) Research Center, the University of North Carolina at Charlotte, Charlotte, NC 28223, USA

[5]SolidEnergy Systems Corp., Woburn, MA 01801, USA

[6]Lead contact

*Correspondence: glenn.r.pastel.civ@army.mil

https://doi.org/10.1016/j.joule.2024.02.002

Please cite this article in press as: Pastel et al., Designing interphases for highly reversible aqueous zinc batteries, Joule (2024), https://doi.org/10.1016/j.joule.2024.02.002

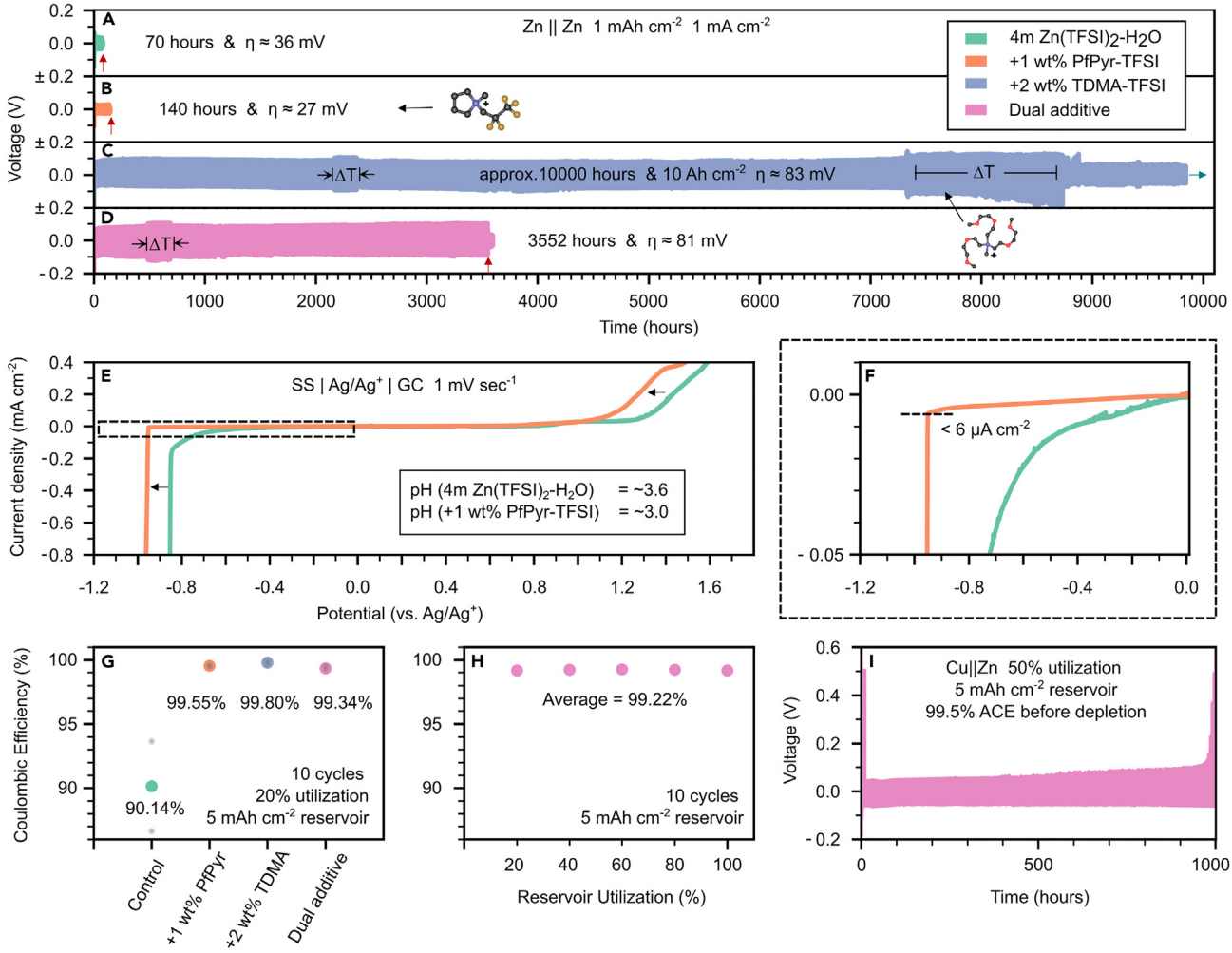

Figure 1. Dendrite susceptibility, parasitic reactions, and reversibility of PfPyr and TDMA co-cations with Zn metal anodes

(A–F) Investigation of dendrite susceptibility with Zn||Zn symmetric cells and (A) the baseline electrolyte 3.8 m $Zn(TFSI)_2$-H_2O, (B) +1 wt % PfPyr, (C) +2 wt % TDMA, and (D) a dual additive composition. (E and F) Cathodic and anodic LSV curves of the baseline and +1 wt % PfPyr electrolytes on SS316 at 1 mV sec^{-1} scan rates.

(G) A comparison of the Coulombic efficiency of the four compositions using duplicate cells (gray points) with an Aurbach protocol and a 5 mAh cm^{-2} reservoir for 10 cycles with 20% reservoir utilization.

(H) The Coulombic efficiency of the dual additive electrolyte with up to 100% reservoir utilization.

(I) Galvanostatic cycling of a Cu||Zn cell with 50% utilization of a 5 mAh cm^{-2} reservoir at 1 mA cm^{-2} current density for 1,000 h.

contradicting the behavior expected for an electrolyte with a marginally lower pH. On the other hand, TDMA does not have a significant impact on parasitic HER with a background current of around 140 μA cm^{-2} before Zn deposition. This behavior hints at competing mechanisms for the two co-cations, neither of which contributes to the widening of the electrochemical stability window of the electrolytes but instead impact the interphase chemistry before and during deposition.

Cycling efficiency

Duplicate half-cell reversibility tests, derived from an Aurbach protocol[22] with 20% utilization per step, indicate an increase in Coulombic efficiency (CE) above 99.5% with both additives (Figure 1). This increase in CE is sustained at higher reservoir utilizations up to 100% for the dual additive composition relative to a stepwise

Please cite this article in press as: Pastel et al., Designing interphases for highly reversible aqueous zinc batteries, Joule (2024), https://doi.org/10.1016/j.joule.2024.02.002

decrease for the composition with only the control and PfPyr (Figure S10). Furthermore, Cu||Zn cells with the dual co-cation electrolyte cycle for over 1,000 h before depleting the initial 5 mAh cm^{-2} reservoir with 50% reservoir utilization, which corresponds to an average CE of 99.5%, assuming minimal loss of Zn to corrosion reactions, as derived from Equation S1 (Figures 1I and S11–S15). This result aligns well with the 99.5% CE achieved by cells cycled with 20% reservoir utilization, which last for over 1,500 h before depletion of the reservoir. This approach facilitates a more accurate determination of CE than asymmetric cells cycled against an impractical counter electrode (Figure S16).[2] The performance enabled by additive levels (3 wt %) of PfPyr and TDMA is unparalleled and strongly implies the direct alteration of interfacial structure and interphase chemistry rather than changes in the bulk Zn^{2+} solvation sheath.

Reaction mechanisms

Previously identified decomposition reactions for room temperature ionic liquids (RTILs) in the presence of a nucleophile/base, such as $TFSI^-$ or OH^-, include the reverse Menshutkin reaction and the Hoffman elimination reaction.[23] In the former, a quaternary ammonium cation reacts with a nucleophilic $TFSI^-$ or OH^- to form R–X and a tertiary amine. The source of OH^- in these electrolytes is suspected to be HER, which is still prevalent. In the latter, a β-hydrogen is eliminated from the quaternary ammonium to form an alkene. In a subsequent reaction, especially in relatively acidic electrolytes or in the presence of Zn^{2+} acting as a Lewis acid, the alkene may be hydrated to form an alcohol. Reaction free energies computed with density functional theory (DFT) are shown in Figure 2A for the (1) reverse Menshutkin and (2) Hoffman elimination with subsequent hydration mechanisms. For TDMA, both mechanisms yield the same tertiary amine and hydroxypolyether product. Following from previous work, the tertiary amine can participate in solid electrolyte interphase (SEI) formation through conversion of dissolved CO_2 to carbonates or hydroxylating exposed ZnO.[24] For PfPyr, however, the Hoffman elimination mechanism opens up the ring, and subsequent hydration of the alkene produces a unique alcohol species compared with the reverse Menshutkin reaction. Electrochemical stability windows predicted using DFT calculations are shown in Figure 2B. These results suggest that it is unlikely that the cations or any of the decomposition products considered here are electrochemically reduced during cycling. Consequently, electrochemical reduction of $TFSI^-$ is the most likely source of fluorine-containing SEI products.[14] However, all three tertiary amine products have relatively low oxidation potentials in the range of 1.25–1.4 V. Therefore, oxidation at the cathode and/or carbonate formation could be limiting factors in certain full-cell chemistries.

In situ shell-isolated nanoparticle-enhanced Raman spectroscopy (SHINERS) reveals that both co-cations have limited impact on the bulk and interphasial solvation behavior of $TFSI^-$ anions in the electrolyte (Figures S17–S19). Negligible shifts in the $TFSI^-$ breathing and other modes are observed throughout *in situ* measurements of three-electrode cells during cyclic voltammetry scans to −1.0 V vs. Ag/AgCl. Slight redshifts in the $TFSI^-$ breathing mode (~1 cm^{-1}) relative to the baseline electrolyte are noted for interphasial measurements with the TDMA additive, as well as for bulk measurements with high weight percentages of the PfPyr additive (4 wt %) (Figures S20 and S21). These observations suggest that the role of PfPyr may be more related to slight perturbations of the bulk $TFSI^-$ solvation structure, whereas the effect of TDMA is likely constrained to the interface, although more investigation is needed to understand the extent of either effect.[6,25] The lack of new peaks at low reduction potentials diminishes the importance of additive decomposition during the initial deposition of Zn^0. Negligible shifts are also observed for the broad O–H

Please cite this article in press as: Pastel et al., Designing interphases for highly reversible aqueous zinc batteries, Joule (2024), https://doi.org/10.1016/j.joule.2024.02.002

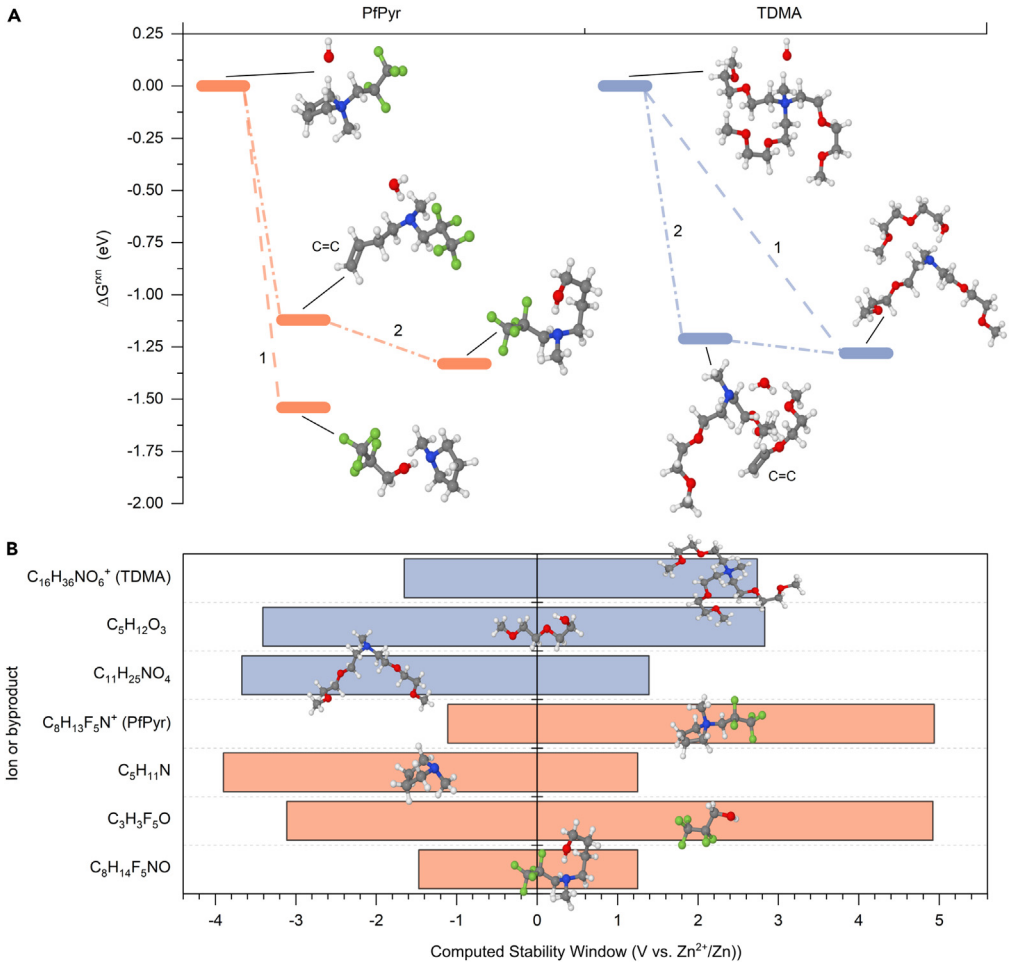

Figure 2. Reaction mechanisms and electrochemical stability predicted by density functional theory

(A) Reaction free energies in eV predicted by density functional theory for $PfPyr^+ + OH^-$ and $TDMA^+ + OH^-$. In both cases, dashed connecting lines labeled "1" highlight the reverse Menshutkin reaction, while the dot-dashed connecting lines labeled "2" highlight Hoffman elimination with subsequent hydration. In the case of $TDMA^+$, the final product of both reactions is the same.

(B) Density functional theory predicted electrochemical stability windows for TDMA, PfPyr, and products resulting from OH^--induced decomposition of the cations. Voltages are reported in the Zn^{2+}/Zn scale. TDMA and its products are shown in orange, while PfPyr and its products are shown in green. There is no significance to the ordering presented.

stretching band in the IR spectra generally associated with three populations of water molecules: multimer, intermediate, and network water (Figures S22–S24). Therefore, neither additive strongly impacts the bulk solvation behavior of water or the interphasial and bulk behavior of $TFSI^-$ anions in the diffuse layer of the electrolyte, as in previous reports for surface-absorbed additives.[26,27] Instead, both co-cations directly impact the surface chemistry and reversibility of the Zn^0 anode by participating in layered double hydroxide (LDH) formation and the proposed HER-driven reactions.

Surface chemistry

X-ray photoelectron spectroscopy (XPS) analysis of sputter depth profiled Zn deposits retrieved after Aurbach CE tests indicate a strong divergence in SEI composition in the presence of either co-cation (Figures 3 and S25–S29). Furthermore, crystalline species delineated by *ex situ* XRD indicate the presence of a LDH with

Please cite this article in press as: Pastel et al., Designing interphases for highly reversible aqueous zinc batteries, Joule (2024), https://doi.org/10.1016/j.joule.2024.02.002

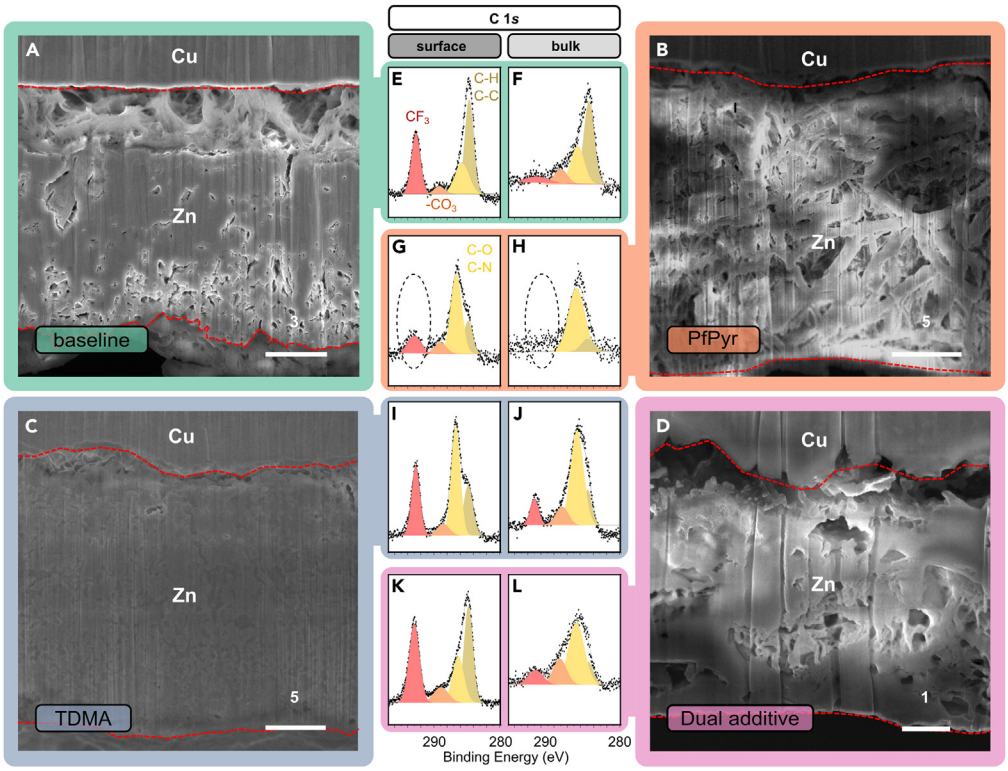

Figure 3. Chemical and morphological effects of co-cations on Zn stripping and plating

XPS and FIB-SEM characterization of 5 mAh cm^{-2} Zn^0 deposits on Cu substrates following an Aurbach Coulombic efficiency test with 20% reservoir utilization at 1 mA cm^{-2} current density. The FIB cross sections (A–D) reveal striking differences in morphology between the four electrolyte compositions, while the surface and bulk C 1*s* spectra (E–L) reveal distinct differences in the LDH and deposit chemistry.

$Zn(TFSI)_2[Zn(OH)_2)]_3 \cdot nH_2O$ as the majority species (Figure S30).[28,29] In XPS, the presence of a LDH is noted by the prominent CF_3 peaks in the topmost scan, corresponding to the surface of the unwashed deposit, around 292.8 and 688.3 eV in the C 1*s* and F 1*s* spectra, respectively. All four electrolytes show some evidence for dried LDH formation on the topmost scan; however, the thickness and composition fluctuate. For the baseline electrolyte, the LDH is limited to the topmost scan, with two distinct peaks in the O 1*s* and Zn 2*p* spectra around 530.4 and 1,021 eV indicative of ZnO further into the deposit.[30] The C 1*s* spectra of the baseline electrolyte also contains peaks around 289.1, 286.8, and 284.8 eV representative of steady anion decomposition,[14] with high intensity relative to the Zn^0 peak around 1,023 eV.

PfPyr transforms the chemical composition of the deposit, most notably with fewer anion decomposition products. More specifically, the signal strength of CF_3, ZnF_2, C=O, and C–H/C–C bonds are all substantially reduced relative to the Zn^0 peak around 1,023 eV. This hints at a deposit with a homogeneous, fluorine-poor composition due to the limited involvement of parasitic reactions.[31] In contrast, TDMA produces a strong CF_3 signal that persists throughout the depth profiling scans around 292.5 eV in the C1*s* spectra and around 688.5 eV as a shoulder band in the F1*s* spectra. However, unlike the baseline electrolyte, solitary Zn 2*p* and O 1*s* peaks indicate a more continuous deposit without ZnO or $ZnCO_3$ formation. The persistent CF_3 signal in the TDMA-containing electrolyte could be indicative of a thicker and more anion-rich LDH. This is further supported by XRD measurements of the deposit, which indicate numerous additional peaks between 10° and 35°, unmatched in the

LDH of the baseline electrolyte. The deposit formed in the presence of both co-cations displays a similar composition to the TDMA additive except for weaker C1s bands in subsequent depth profiling scans relative to the Zn^0 signal and weaker diffraction signal of the interphase species.

Morphology

Zinc morphology is revealed by focused ion beam scanning electron microscopy (FIB-SEM) cross section and top view images of the samples prepared under identical conditions for XPS (Figures 3 and S31). The baseline electrolyte produces a deposit with varied morphology perpendicular to the copper substrate. On the substrate, the deposit is highly porous due to proliferate anion decomposition and trapping of LDH species with a thick zinc metal deposit plated on top. The zinc deposit becomes more porous, again, farther away from the copper substrate, indicating an increase in dendrite susceptibility with anode loading and utilization. In contrast, the PfPyr deposit is highly porous and tortuous throughout, with large isotropic deposits around 1 μm in diameter. This surprising result hints at the trade-off that often exists between improvements in deposition purity and morphology. The corresponding top view image of the LDH layer of the PfPyr electrode also reveals fewer crystalline species than the TDMA electrolyte samples, in agreement with XRD.

The TDMA deposit is the densest of all the compositions with relatively good attachment to the copper substrate, characteristic of the long cycle lifetimes in previous anode reversibility tests. The dual co-cation cross section reveals a morphology that shares similarities with both PfPyr- and TDMA-originated deposits. The thin deposit contains areas with high porosity and high density, which likely indicates competition between the two co-cations to dominate the surface chemistry and morphology. Transmission electron microscopy (TEM) images of the corresponding Zn counter electrodes indicate a thick SEI after 30 h of cycling with competition between amorphous and polycrystalline species associated with the PfPyr and TDMA co-cation, respectively (Figure S32).[8,32] In summary, the morphology of the Zn^0 deposits helps confirm the differences in performance between these two co-cation chemistries. Their small weight percentages in the electrolytes have a disproportional impact on the deposition morphology of Zn^0 in slightly acidic aqueous electrolytes.

Full-cell demonstrations

Prototype full cells were prepared using three different cathode chemistries including O_2, polyaniline (PANI) organic cathode, and a $HNaV_6O_{16}$ (NVO) inorganic cathode (Figure 4; Table S3). Zn-air batteries promise high volumetric energy density as primary cells, but separate challenges associated with anode and cathode reversibility have largely impeded rechargeable configurations. $Zn||O_2$ cells with the combined co-cation electrolyte last almost twice as long as control cells during continuous cycling at 0.5 and 1 mAh cm^{-2} (Figure S33). However, cells with just the TDMA co-cation perform better than those with PfPyr, lasting for over 100 cycles or 400 h, under the same conditions with lower overpotentials. These prototypes demonstrate that each co-cation can be leveraged independently or in combination without adversely impacting performance. Further optimization of the zinc air prototypes is warranted but is beyond the scope of this study.

An organic cathode based on the oxidation and reduction of the emeraldine base of PANI demonstrates impressive cycling stability in the dual additive electrolyte for over 600 cycles at high areal capacities around 1.5 mAh cm^{-2} and 10 μl mg^{-1} electrolyte loading. As the capacitive electrode[33–35] activates during the first 50 cycles,[36]

Please cite this article in press as: Pastel et al., Designing interphases for highly reversible aqueous zinc batteries, Joule (2024), https://doi.org/10.1016/j.joule.2024.02.002

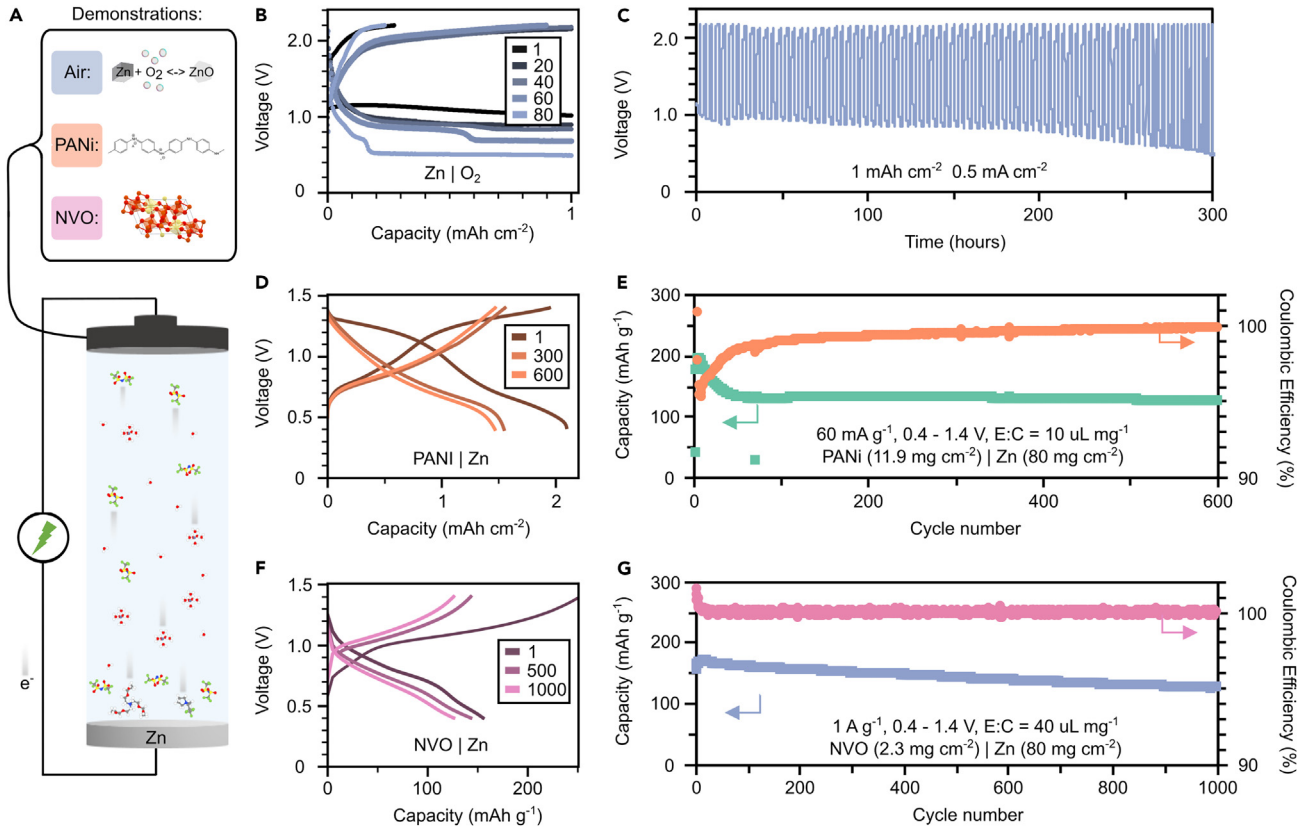

Figure 4. Full-cell demonstrations with O_2, polyaniline, and $HNaV_6O_{16}$ cathodes

(A) A schematic depicting the investigation of three full-cell chemistries including (B and C) O_2, (E and F) an organic cathode, and (G and H) an inorganic cathode to confirm the compatibility of the additives under different cathode storage mechanisms.

(B–D) Zn||O_2 cells demonstrate over 300 h of continuous cycling at 0.5 and 1 mAh cm^{-2}. Gradual formation of ZnO in the air cathode limits reversibility after 80 cycles.

(E and F) An organic cathode based on the oxidation and reduction of the emeraldine base of polyaniline (PANI) demonstrates impressive cycling stability with the cation additives for over 500 cycles at high areal capacities around 1.5 mAh cm^{-2}.

(G and H) An inorganic $HNaV_6O_{16}$ (NVO) cathode displays excellent rate performance based on proton insertion at 1 A g^{-1} for over 1,000 cycles with 99.95% average Coulombic efficiency.

the cathode delivers capacities of 132 mAh g^{-1} or energy density of 126 Wh kg^{-1}, which drop to 124 mAh g^{-1} or 80 Wh kg^{-1} over the next 600 cycles with an average CE of 99.3% (Figure S34). By continuously cycling for over 3 months with high areal capacity at a commercially relevant rate (~C/2 or 60 mA g^{-1}), this performance stands out when compared with previous reports.[32–35]

An inorganic, dry-coated cathode with the highest areal capacity (5 mAh cm^{-2}) ever reported for NVO, at a commercially relevant rate (1.5 mA cm^{-2}), was successfully demonstrated for a limited number of cycles with the dual co-cation electrolyte (Figure S35). The thick laminate (30.4 mg cm^{-2}, 80% active) achieves good gravimetric capacity (200 mAh g^{-1}) and is well suited for further optimization in subsequent studies. A lower-loading laminate (2.3 mg cm^{-2} active) displays excellent reversibility at a higher rate for over 1,000 cycles with 81% capacity retention and 99.95% average CE (Figures 4F and 4G). The initial capacity of the cathode at 1 A g^{-1} is 156 mAh g^{-1} (117 Wh kg^{-1}) with −0.019% capacity loss per cycle over 1,000 cycles. In sharp contrast, full cells with the baseline electrolyte dropped to < 80% capacity retention within 50 cycles (Figure S36). While the storage

Please cite this article in press as: Pastel et al., Designing interphases for highly reversible aqueous zinc batteries, Joule (2024), https://doi.org/10.1016/j.joule.2024.02.002

mechanism of NVO and similar V_xO_y cathodes is still contested, both co-insertion of H^+ along with Zn^{2+} and conversion processes based on layered hydroxide formation offer poor calendar life, which require additional consideration.[37]

DISCUSSION

In this work, two co-cations with complementary functions for aqueous zinc batteries were synthesized and investigated. These co-cations demonstrate that key metrics of electrochemical performance in aqueous Zn electrolytes can be directly and efficiently controlled via interphasial engineering without altering Zn^{2+} solvation. A partially fluorinated pyrrolidinium suppresses parasitic reactions but produces tortuous deposits somewhat susceptible to dendrite formation. The ether-functionalized ammonium promotes more uniform Zn^0 morphology, thereby limiting dendrite formation, at the expense of additional anion reduction and thick LDH formation. Full-cell demonstrations produce promising performance with multiple cathode chemistries and contrasting storage mechanisms. However, in each demonstration, significant improvements in performance are realized with only additive levels of each cation to engineer the respective Zn metal interphases. Future work can apply similar co-cation compositions with mixed anions, mixed solvents, or high-entropy electrolytes to further improve performance and balance the interphase behavior of metal anodes. By further exploring cheaper and more environmentally friendly anions and other functional groups, co-cations can become a keystone of future high-performance electrolytes.

EXPERIMENTAL PROCEDURES

Resource availability

Lead contact

Further information and requests for resources and materials should be directed to the lead author, Dr. Glenn Pastel (glenn.r.pastel.civ@army.mil).

Materials availability

The materials in this study can be made available upon reasonable request.

Data and code availability

The datasets generated in this study are available upon reasonable request.

Materials

1-Methyl-1-(2,2,3,3,3-pentafluoropropyl)pyrrolidinium bis(trifluoromethylsulfonyl) imide (PfPyr). The synthesis involves three-steps to prepare and react 1-(2,2,3,3,3-pentafluoropropyl)pyrrolidine with CH_3TFSI as previously reported in the literature.[18]

Tris(3,6-dioxaheptanyl)(methyl)ammonium bis(trifluoromethylsulfonyl)imide (TMDA)

The synthesis involves a two-step reaction. In the first step, a pressure vessel is charged with tris[2-(2-methoxyethoxy)ethyl]amine, dimethyl carbonate, and methanol; stirred; and heated up to 120°C for 12 h. In the second step, the product is titrated with bis(trifluoromethanesulfonyl)imide acid (HTFSI) under constant stirring until the pH drops below 7. Then the product is refluxed with active carbon (10 g) in an acetonitrile solution for 2 h to remove residual impurities. The active carbon is removed by filtration, and a light amber ionic liquid is yielded after drying at 60°C under vacuum for 24 h.

Please cite this article in press as: Pastel et al., Designing interphases for highly reversible aqueous zinc batteries, Joule (2024), https://doi.org/10.1016/j.joule.2024.02.002

Electrolyte

Solutions were prepared by dissolving $Zn(TFSI)_2$ in deionized water (18 kΩ) and adding the correct concentration of the co-cations in an Ar-filled glovebox. The dual additive electrolyte referenced throughout this work consisted of 3.8 m $Zn(TFSI)_2$ in H_2O with 1 wt % PfPyr and 2 wt % TDMA. Zinc bis(trifluoromethylsulfonyl)imide ($Zn(TFSI)_2$) was used as received from various vendors (TCI Chemicals or Solvoionic, purity > 99%). Our experiments indicate that no more than 4 wt % of the PfPyr additive is soluble in the baseline electrolyte with an optimized loading of 1 wt %. The TDMA additive is a RTIL and miscible with water up to high concentrations.

Electrodes

Zn and Cu foil are used as received from various vendors without additional pretreatment (MSE Supplies, 100 μm, purity > 99%). Positive electrodes for Zn||O_2 cells are prepared from gas diffusion electrodes (Sigracet 39BB, Fuel Cell Store) with around 1 mg cm^{-2} of catalyst. The catalyst ink consists of 90 wt % platinum black (nominally 40% Pt, Alfa Aesar) and 10 wt % Nafion (Sigma) in isopropyl alcohol and water (50/50 wt %). The ink was pulse sonicated for 20 min, then drop cast on the gas diffusion layer (GDL), and dried overnight at 120°C. $Na_2V_6O_{16}{\cdot}nH_2O$ (NVO)-positive electrode material was synthesized based on previous reports.[13] NVO slurries were prepared by mixing NVO (70 wt %), Timcal C45 (20 wt %), and polyvinylidene fluoride (PVDF) (10 wt %) in N-methylpyrrolidone (NMP, Alfa Aesar) in a SPEX 5120 Mixer/Mill at 750 rpm for 5 × 2 min. The slurry was doctor bladed with a 300 μm gap height on Ti foil (MSE Supplies, 100 μm) and dried overnight at 80°C. Laminate loading is between 3 to 5 mg cm^{-2}. Thick, dry-coated NVO cathode was prepared by dry-coating NVO (80 wt %), Timcal C45 (8 wt %), carbon nanotubes (CheapTubes, 2 wt %), and polytetrafluoroethylene (PTFE, Sigma, 10 wt %) as previously reported in the literature.[35,38] Laminates were gently calendared down to 275 μm thickness with approximately 30.4 mg cm^{-2} loading. Polyaniline (PANI) positive electrodes were prepared by dry-coating polyaniline (emeraldine base, 100 kMW, Sigma-Aldrich, 70 wt %), Timcal C45 (20 wt %), and PTFE (Sigma, 10 wt %) as previously reported in the literature.[35,38] Laminates were calendared down to 270 μm thickness with approximately 15 mg cm^{-2} mass loading.

Electrochemical measurements

Coin cells were fabricated with SS316 2032-sized cases (MTI), one 19-mm diameter glass fiber layer (Whatman QMF), two 19-mm diameter Celgard 3501 layers, 1 mm of spacers, one spring, and 110–150 μL electrolyte in an Ar-filled glovebox or dry room (dew point < −30°C). Zn||O_2 were prepared by a two-step approach. In the first step, coin cells with porous top caps (MTI), Teflon film, Ni foam, gas diffusion layer, one glass fiber layer, two Celgard 3501 layers, 1 mm of spacers, one spring, and 150 μL electrolyte were stacked without crimping and evacuated for 10 s after fabrication to improve the wetting of the electrodes. In the second step, cells were placed in holder with Ni tabs and sealed in a pouch bag to insulate from changes in humidity and air composition, with around 10 mL of additional O_2. All galvanostatic cycling protocols were performed on a 64-channel Neware BTS with a constant temperature chamber set to 30°C or at room temperature for Zn||O_2 cells. Three-electrode beaker cells for cyclic and LSV experiments were performed with a Biologic SP-150, with electrodes spaced 100 μm apart, without a rigid separator layer, with 400 μL of electrolyte, with stainless-steel 316 working electrodes, with glassy carbon counter electrodes, and with either a Ag/AgCl or Hg/HgO reference electrodes at 1 mV s^{-1} scan rates. Please note that the separator strongly influences the performance, and previous work has pointed out the importance of both microporous and non-woven layers, as adopted in this work.[39,40]

Please cite this article in press as: Pastel et al., Designing interphases for highly reversible aqueous zinc batteries, Joule (2024), https://doi.org/10.1016/j.joule.2024.02.002

Material characterization

Raman spectroscopy and SHINERS were conducted using a confocal inVia Reflux Raman micro-spectrometer equipped with a 10× microscope objective. For sample excitation, a 1,800 grooves/mm diffraction grating and 100% laser power were used. The excitation wavelength was 633 nm. Background correction was performed using Wire 4.0 software. Enhanced Raman measurements utilized shell-isolated nanoparticles (SHINs) synthesized in-house.[41] These SHINs consisted of a 60-nm diameter Au nanoparticle core enveloped by a 2-nm-thick silica (SiO_2) shell, enhancing the surface signal. The synthesis of these SHINs adhered to established procedures found in the literature. X-ray photoelectron spectra were acquired with a PHI Versaprobe III after preparing samples in an Ar-filled glovebox and drying under vacuum overnight. Samples were extracted from half cells after Aurbach CE tests performed with a 5 mAh cm^{-2} reservoir and 20% utilization for ten cycles at 1 mA cm^{-2} without washing or mechanically abrading the respective surface. Spectra were collected by using a combination of survey (224 eV pass energy, 0.5 eV step size) and high-resolution scans (22 eV pass energy, 0.05 eV step size) with a 100 μm X-ray spot size and 25 W power. Sputter depth profiling with 3–5 min intervals used a 500 V Ar^+ beam with a 3 × 3 mm region. Peak fitting was performed using PHI's Multipak software v. 9.6 with 70/30 Gaussian/Lorentzian line shapes on a Shirley background. Spectra were shifted relative to the binding energy of C1s sp^3 at 284.8 eV or ZnF_2 around 685.0 eV. ^1H, ^{13}C, and ^{19}F solution-state nuclear magnetic resonance spectra were acquired with a Magritek Spinsolve Carbon with $CDCl_3$. Focused ion beam and scanning electron microscopy images were collected with a Tescan XEIA FEG SEM by Dr. Jiancun Rao at the University of Maryland AIMLab. Samples were extracted and prepared by the same methods as for XPS characterization. X-ray diffraction spectra were collected with a Rigaku Miniflex system between 3° and 90° with a 10° min^{-1} scan rate. Infrared spectra were collected by averaging 256 scans with 4 cm^{-1} resolution in an attenuated total internal reflection geometry with a Nicolet 6700 spectrometer (Thermo Scientific). pH and conductivity measurements were performed with FiveEasy pH/mV and Conductivity meters (Mettler Toledo) after routine calibration with 1.68, 4.00, 7.00, and 10.00 pH solutions.

Computational methods

An in-house script was used to perform an initial conformer search with rdkit using the MMFF94 force field, querying structures cid: 156497211 (PfPyr) and cid: 21133406 (TDMA) from PubChem.[42,43] The lowest energy structures from this search were used to seed additional searches using Crest—though the most extended conformer of TDMA is also used to seed further conformer searches.[44] The process was repeated for decomposition byproducts with PubChem cids: 8134, 8454, 9872, 90799598, and a molecule with canonical SMILES CN(CCCCO)CC(F)(F)C(F)(F)F (no PubChem entry). For reactions, Crest was used to sample myriad dimer configurations with OH^- or H_2O—in the latter case, an H is removed from the TDMA or PfPyr molecule. Reaction free energies are computed as free energy differences between related products and reactants and are expressed in units of eV throughout the text. Reduction and oxidation potentials for TDMA, PfPyr, and their decomposition products are computed using the Nernst equation:

$$E^{redox} = \pm\frac{\Delta G(A^{\pm}) - \Delta G(A)}{nF} - 3.68\ V$$

where, $\Delta G(A^{\pm}) - \Delta G(A)$ is the free energy difference between the reduced or oxidized species and the cation or solvent molecule, n is the number of electrons transferred (=1 in this case), F is Faraday's constant, and −3.68 V shifts the potential to the Zn^{2+}/Zn scale, assuming a value of 4.44 V for the absolute standard hydrogen electrode potential and −0.76 V for the standard reduction potential of zinc. Free energies are

Please cite this article in press as: Pastel et al., Designing interphases for highly reversible aqueous zinc batteries, Joule (2024), https://doi.org/10.1016/j.joule.2024.02.002

computed at the M05-2X/6-31+G(d,p) level of theory with the SMD implicit solvation method and acetone dielectric (widely used to mimic reduced dielectric in aqueous battery electrolytes) with Gaussian 16 rev. C.02.[45–47] Inputs are prepared with the atomic simulation environment.[48] Images prepared with Jmol and rendered with POVRay 3.7.[49]

SUPPLEMENTAL INFORMATION

Supplemental information can be found online at https://doi.org/10.1016/j.joule.2024.02.002.

ACKNOWLEDGMENTS

This research was led by researchers within the Joint Center for Energy Storage Research (JCESR), an Energy Innovation Hub funded by the US Department of Energy (DOE), Office of Science, Basic Energy Sciences (BES). G.R.P. is grateful for discussions with Dr. Adelaide Nolan and Dr. Jeffrey Read. L.M. acknowledges support from the US National Science Foundation Award No. 2301719. Additionally, support for this work by the US Department of the Army and DEVCOM Army Research Lab is gratefully acknowledged. This paper describes objective technical results and analysis. Any subjective views or opinions that might be expressed in the paper do not necessarily represent the views of the US Department of Defense or the United States Government.

AUTHOR CONTRIBUTIONS

G.R.P., conceptualization, data curation, formal analysis, investigation, project administration, visualization, writing; T.P.P., data curation, formal analysis, investigation, software, visualization, writing; Q.L., data curation, investigation; S.L., data curation, formal analysis, writing – review; Q.Z., data curation, investigation; R.J., formal analysis, investigation; L.M., formal analysis, writing – review; J.C., formal analysis, writing – review; O.B., formal analysis, resources, supervision, writing – review; M.A.S., formal analysis, investigation, supervision, writing; Z.Z., resources, supervision, writing – review; K.X., funding acquisition, project administration, resources, supervision, writing – review.

DECLARATION OF INTERESTS

G.R.P., T.P.P., Q.L., O.B., M.A.S., Z.Z., and K.X. filed provisional patents on the PfPyr and TDMA additives.

Received: September 27, 2023
Revised: October 23, 2023
Accepted: February 1, 2024
Published: February 23, 2024

REFERENCES

1. Parker, J.F., Ko, J.S., Rolison, D.R., and Long, J.W. (2018). Translating Materials-Level Performance into Device-Relevant Metrics for Zinc-Based Batteries. Joule *2*, 2519–2527.

2. Ma, L., Schroeder, M.A., Pollard, T.P., Borodin, O., Ding, M.S., Sun, R., Cao, L., Ho, J., Baker, D.R., Wang, C., et al. (2020). Critical Factors Dictating Reversibility of the Zinc Metal Anode. Energy & Environ. Materials *3*, 516–521.

3. Li, C., Jin, S., Archer, L.A., and Nazar, L.F. (2022). Toward practical aqueous zinc-ion batteries for electrochemical energy storage. Joule *6*, 1733–1738.

4. Xu, K. (2014). Electrolytes and Interphases in Li-Ion Batteries and Beyond. Chem. Rev. *114*, 11503–11618.

5. Parker, J.F., Pala, I.R., Chervin, C.N., Long, J.W., and Rolison, D.R. (2016). Minimizing Shape Change at Zn Sponge Anodes in Rechargeable Ni–Zn Cells: Impact of Electrolyte Formulation. J. Electrochem. Soc. *163*, A351–A355.

6. Zhang, Y., Wan, G., Lewis, N.H.C., Mars, J., Bone, S.E., Steinrück, H.-G., Lukatskaya, M.R., Weadock, N.J., Bajdich, M., Borodin, O., et al. (2021). Water or Anion? Uncovering the Zn^{2+} Solvation Environment in Mixed $Zn(TFSI)_2$ and LiTFSI Water-in-Salt Electrolytes. ACS Energy Lett. *6*, 3458–3463.

7. Zhang, S.S. (2006). A review on electrolyte additives for lithium-ion batteries. J. Power Sources *162*, 1379–1394.

8. Cao, L., Li, D., Pollard, T., Deng, T., Zhang, B., Yang, C., Chen, L., Vatamanu, J., Hu, E., Hourwitz, M.J., et al. (2021). Fluorinated interphase enables reversible aqueous zinc battery chemistries. Nat. Nanotechnol. *16*, 902–910.

9. Sun, P., Ma, L., Zhou, W., Qiu, M., Wang, Z., Chao, D., and Mai, W. (2021). Simultaneous

Regulation on Solvation Shell and Electrode Interface for Dendrite-Free Zn Ion Batteries Achieved by a Low-Cost Glucose Additive. Angew. Chem. Int. Ed. Engl. *60*, 18247–18255.

10. Hao, J., Yuan, L., Zhu, Y., Jaroniec, M., and Qiao, S.Z. (2022). Triple-Function Electrolyte Regulation toward Advanced Aqueous Zn-Ion Batteries. Adv. Mater. *34*, e2206963.

11. Han, D., Wang, Z., Lu, H., Li, H., Cui, C., Zhang, Z., Sun, R., Geng, C., Liang, Q., Guo, X., et al. (2022). A Self-Regulated Interface toward Highly Reversible Aqueous Zinc Batteries. Adv. Energy Mater. *12*, 2102982.

12. Zhao, K., Fan, G., Liu, J., Liu, F., Li, J., Zhou, X., Ni, Y., Yu, M., Zhang, Y.M., Su, H., et al. (2022). Boosting the Kinetics and Stability of Zn Anodes in Aqueous Electrolytes with Supramolecular Cyclodextrin Additives. J. Am. Chem. Soc. *144*, 11129–11137.

13. Ma, L., Pollard, T.P., Zhang, Y., Schroeder, M.A., Ding, M.S., Cresce, A.V., Sun, R., Baker, D.R., Helms, B.A., Maginn, E.J., et al. (2021). Functionalized Phosphonium Cations Enable Zinc Metal Reversibility in Aqueous Electrolytes. Angew. Chem. *133*, 12546–12553.

14. Ma, L., Pollard, T.P., Zhang, Y., Schroeder, M.A., Ren, X., Han, K.S., Ding, M.S., Cresce, A.V., Atwater, T.B., Mars, J., et al. (2022). Ammonium enables reversible aqueous Zn battery chemistries by tailoring the interphase. One Earth *5*, 413–421.

15. Ma, L., Vatamanu, J., Hahn, N.T., Pollard, T.P., Borodin, O., Petkov, V., Schroeder, M.A., Ren, Y., Ding, M.S., Luo, C., et al. (2022). Highly reversible Zn metal anode enabled by sustainable hydroxyl chemistry. Proc. Natl. Acad. Sci. USA *119*, e2121138119.

16. McMillan, R., Slegr, H., Shu, Z.X., and Wang, W. (1999). Fluoroethylene carbonate electrolyte and its use in lithium ion batteries with graphite anodes. Journal of Power Sources *81–82*, 20–26.

17. Wang, C., Meng, Y.S., and Xu, K. (2019). Perspective—Fluorinating Interphases. J. Electrochem. Soc. *166*, A5184–A5186.

18. Liu, Q., Hsu, C.W., Dzwiniel, T.L., Pupek, K.Z., and Zhang, Z. (2020). A fluorine-substituted pyrrolidinium-based ionic liquid for high-voltage Li-ion batteries. Chem. Commun. (Camb) *56*, 7317–7320.

19. Liu, Q., Jiang, W., Xu, J., Xu, Y., Yang, Z., Yoo, D.J., Pupek, K.Z., Wang, C., Liu, C., Xu, K., et al. (2023). A fluorinated cation introduces new interphasial chemistries to enable high-voltage lithium metal batteries. Nat. Commun. *14*, 3678.

20. Xu, K. (2023). Electrolytes, Interfaces and Interphases: Fundamentals and Applications in Batteries (Royal Society of Chemistry).

21. Aurbach, D., and Granot, E. (1997). The study of electrolyte solutions based on solvents from the "glyme" family (linear polyethers) for secondary Li battery systems. Electrochim. Acta *42*, 697–718.

22. Aurbach, D., Gofer, Y., and Langzam, J. (1989). The Correlation Between Surface Chemistry, Surface Morphology, and Cycling Efficiency of Lithium Electrodes in a Few Polar Aprotic Systems. J. Electrochem. Soc. *136*, 3198–3205.

23. Kar, M., Winther-Jensen, B., Armand, M., Simons, T.J., Winther-Jensen, O., Forsyth, M., and MacFarlane, D.R. (2016). Stable zinc cycling in novel alkoxy-ammonium based ionic liquid electrolytes. Electrochim. Acta *188*, 461–471.

24. Cao, C., Pollard, T.P., Borodin, O., Mars, J.E., Tsao, Y., Lukatskaya, M.R., Kasse, R.M., Schroeder, M.A., Xu, K., Toney, M.F., et al. (2021). Toward Unraveling the Origin of Lithium Fluoride in the Solid Electrolyte Interphase | Chemistry of Materials. Chem. Mater. *33*, 7315–7336.

25. Driscoll, D.M., Lavan, S.N., Zorko, M., Redfern, P.C., Ilic, S., Agarwal, G., Fister, T.T., Assary, R.S., Cheng, L., Strmcnik, D., et al. (2023). Emergent solvation phenomena in non-aqueous electrolytes with multiple anions. Chem *9*, 1955–1971.

26. Huang, C., Zhao, X., Liu, S., Hao, Y., Tang, Q., Hu, A., Liu, Z., and Chen, X. (2021). Stabilizing Zinc Anodes by Regulating the Electrical Double Layer with Saccharin Anions. Adv. Mater. *33*, e2100445.

27. Zhu, K., Guo, C., Gong, W., Xiao, Q., Yao, Y., Davey, K., Wang, Q., Mao, J., Xue, P., and Guo, Z. (2023). Engineering an electrostatic field layer for high-rate and dendrite-free Zn metal anodes. Energy Environ. Sci. *16*, 3612–3622.

28. Rajabi, R., Sun, S., Billings, A., Mattick, V.F., Khan, J., and Huang, K. (2022). Insights into Chemical and Electrochemical Interactions between Zn Anode and Electrolytes in Aqueous Zn−ion Batteries. J. Electrochem. Soc. *169*, 110536.

29. Jin, Y., Zou, L., Liu, L., Engelhard, M.H., Patel, R.L., Nie, Z., Han, K.S., Shao, Y., Wang, C., Zhu, J., et al. (2019). Joint Charge Storage for High-Rate Aqueous Zinc–Manganese Dioxide Batteries. Adv. Mater. *31*, e1900567.

30. Frankcombe, T.J., and Liu, Y. (2023). Interpretation of Oxygen 1s X-ray Photoelectron Spectroscopy of ZnO. Chem. Mater. *35*, 5468–5474.

31. Steinrück, H.G., Cao, C., Lukatskaya, M.R., Takacs, C.J., Wan, G., Mackanic, D.G., Tsao, Y., Zhao, J., Helms, B.A., Xu, K., et al. (2020). Interfacial Speciation Determines Interfacial Chemistry: X-ray-Induced Lithium Fluoride Formation from Water-in-salt Electrolytes on Solid Surfaces. Angew. Chem. Int. Ed. Engl. *59*, 23180–23187.

32. Zeng, X., Mao, J., Hao, J., Liu, J., Liu, S., Wang, Z., Wang, Y., Zhang, S., Zheng, T., Liu, J., et al. (2021). Electrolyte Design for In Situ Construction of Highly Zn2+-Conductive Solid Electrolyte Interphase to Enable High-Performance Aqueous Zn-Ion Batteries under Practical Conditions. Adv. Mater. *33*, e2007416.

33. Zhang, Y., Liang, Y., Dong, H., Wang, X., and Yao, Y. (2020). Charge Storage Mechanism of a Quinone Polymer Electrode for Zinc-ion Batteries. J. Electrochem. Soc. *167*, 070558.

34. Zhang, Y., Zhao, L., Liang, Y., Wang, X., and Yao, Y. (2022). Effect of electrolyte anions on the cycle life of a polymer electrode in aqueous batteries. eScience *2*, 110–115.

35. Wan, F., Zhang, L., Wang, X., Bi, S., Niu, Z., and Chen, J. (2018). An Aqueous Rechargeable Zinc-Organic Battery with Hybrid Mechanism. Adv. Funct. Mater. *28*, 1804975.

36. Shi, H.-Y., Ye, Y.-J., Liu, K., Song, Y., and Sun, X. (2018). A Long-Cycle-Life Self-Doped Polyaniline Cathode for Rechargeable Aqueous Zinc Batteries. Angew. Chem. *130*, 16597–16601.

37. Wu, J., Yang, Z., and Chen, H. (2022). Oxygen-Deficient $HNaV_6O_{16}{\cdot}4H_2O$@Reduced Graphene Oxide as a Cathode for Aqueous Rechargeable Zinc-Ion Batteries. Ind. Eng. Chem. Res. *61*, 10640–10649.

38. Zhang, Q., Ma, Y., Lu, Y., Li, L., Wan, F., Zhang, K., and Chen, J. (2020). Modulating electrolyte structure for ultralow temperature aqueous zinc batteries. Nat. Commun. *11*, 4463.

39. Garche, J., and Dyer, C.K. (2009). Encyclopedia of Electrochemical Power Sources (Elsevier).

40. Bonnick, P. (2015). Development of a Lab-Scale, Rechargeable, Aqueous Coin Cell and Methods for Measuring the Self-Discharge Rate of Zinc Electrodes. Doctoral dissertation.

41. Li, J.F., Huang, Y.F., Ding, Y., Yang, Z.L., Li, S.B., Zhou, X.S., Fan, F.R., Zhang, W., Zhou, Z.Y., Wu, D.Y., et al. (2010). Shell-isolated nanoparticle-enhanced Raman spectroscopy. Nature *464*, 392–395.

42. rdkit/rdkit (2022). Zenodo*09*. 3 (Q3 2022) Release (Release_2022_09_3). https://zenodo.org/record/7415128.

43. Kim, S., Chen, J., Cheng, T., Gindulyte, A., He, J., He, S., Li, Q., Shoemaker, B.A., Thiessen, P.A., Yu, B., et al. (2023). PubChem 2023 update. Nucleic Acids Res. *51*, D1373–D1380.

44. Pracht, P., Bohle, F., and Grimme, S. (2020). Automated exploration of the low-energy chemical space with fast quantum chemical methods. Phys. Chem. Chem. Phys. *22*, 7169–7192.

45. Gaussian 16. Rev. C.01 (Wallingford, CT, 2016). https://gaussian.com/citation/.

46. Cramer, C.J., and Truhlar, D.G. (2008). A Universal Approach to Solvation Modeling. Acc. Chem. Res. *41*, 760–768.

47. Zhao, Y., Schultz, N.E., and Truhlar, D.G. (2006). Design of Density Functionals by Combining the Method of Constraint Satisfaction with Parametrization for Thermochemistry, Thermochemical Kinetics, and Noncovalent Interactions. J. Chem. Theor. Comput. *2*, 364–382. https://pubs.acs.org/doi/10.1021/ct0502763.

48. Hjorth Larsen, A., Jørgen Mortensen, J., Blomqvist, J., Castelli, I.E., Christensen, R., Dułak, M., Friis, J., Groves, M.N., Hammer, B., Hargus, C., et al. (2017). The atomic simulation environment—a Python library for working with atoms. J. Phys. Condens. Matter *29*, 273002.

49. Hanson, R.M. (2010). *Jmol* – a paradigm shift in crystallographic visualization. J. Appl. Crystallogr. *43*, 1250–1260.